

Measurement of $e^+e^- \rightarrow D_s^{(*)+} D_s^{(*)-}$ cross sections near threshold using initial-state radiation

G. Pakhlova,¹⁷ I. Adachi,¹⁰ H. Aihara,⁵⁰ K. Arinstein,^{1,38} T. Aushev,^{24,17} T. Aziz,⁴⁵ A. M. Bakich,⁴⁴
V. Balagura,¹⁷ E. Barberio,²⁸ A. Bay,²⁴ K. Belous,¹⁶ V. Bhardwaj,⁴⁰ B. Bhuyan,¹³ A. Bondar,^{1,38}
A. Bozek,³⁴ M. Bračko,^{26,18} T. E. Browder,⁹ A. Chen,³¹ P. Chen,³³ B. G. Cheon,⁸ R. Chistov,¹⁷ I.-S. Cho,⁵⁵
K. Cho,²¹ K.-S. Choi,⁵⁵ S.-K. Choi,⁷ Y. Choi,⁴³ J. Dalseno,^{27,46} M. Danilov,¹⁷ Z. Doležal,² A. Drutskoy,⁴
S. Eidelman,^{1,38} D. Epifanov,^{1,38} N. Gabyshev,^{1,38} A. Garmash,^{1,38} B. Golob,^{25,18} H. Ha,²² J. Haba,¹⁰
K. Hayasaka,²⁹ H. Hayashii,³⁰ Y. Horii,⁴⁹ Y. Hoshi,⁴⁸ W.-S. Hou,³³ H. J. Hyun,²³ T. Iijima,²⁹ K. Inami,²⁹
R. Itoh,¹⁰ M. Iwabuchi,⁵⁵ Y. Iwasaki,¹⁰ N. J. Joshi,⁴⁵ T. Julius,²⁸ J. H. Kang,⁵⁵ P. Kapusta,³⁴ H. Kawai,³
T. Kawasaki,³⁶ C. Kiesling,²⁷ H. J. Kim,²³ H. O. Kim,²³ M. J. Kim,²³ S. K. Kim,⁴² Y. J. Kim,⁶ K. Kinoshita,⁴
B. R. Ko,²² S. Korpar,^{26,18} P. Krizan,^{25,18} T. Kumita,⁵¹ A. Kuzmin,^{1,38} Y.-J. Kwon,⁵⁵ S.-H. Kyeong,⁵⁵
J. S. Lange,⁵ M. J. Lee,⁴² S.-H. Lee,²² C. Liu,⁴¹ Y. Liu,³³ D. Liventsev,¹⁷ R. Louvot,²⁴ A. Matyja,³⁴ S. McOnie,⁴⁴
K. Miyabayashi,³⁰ H. Miyata,³⁶ Y. Miyazaki,²⁹ R. Mizuk,¹⁷ G. B. Mohanty,⁴⁵ T. Mori,²⁹ Y. Nagasaka,¹¹
E. Nakano,³⁹ M. Nakao,¹⁰ H. Nakazawa,³¹ S. Nishida,¹⁰ K. Nishimura,⁹ O. Nitoh,⁵² T. Nozaki,¹⁰ S. Ogawa,⁴⁷
T. Ohshima,²⁹ S. Okuno,¹⁹ S. L. Olsen,^{42,9} P. Pakhlov,¹⁷ H. Palka,³⁴ C. W. Park,⁴³ H. Park,²³ H. K. Park,²³
R. Pestotnik,¹⁸ M. Petrič,¹⁸ L. E. Piilonen,⁵³ A. Poluektov,^{1,38} M. Röhrken,²⁰ S. Ryu,⁴² H. Sahoo,⁹ K. Sakai,¹⁰
Y. Sakai,¹⁰ O. Schneider,²⁴ C. Schwanda,¹⁵ K. Senyo,²⁹ M. E. Sevir,²⁸ M. Shapkin,¹⁶ V. Shebalin,^{1,38} C. P. Shen,⁹
J.-G. Shiu,³³ B. Shwartz,^{1,38} F. Simon,^{27,46} P. Smerkol,¹⁸ Y.-S. Sohn,⁵⁵ A. Sokolov,¹⁶ E. Solovieva,¹⁷ S. Stanič,³⁷
M. Starič,¹⁸ T. Sumiyoshi,⁵¹ Y. Teramoto,³⁹ I. Tikhomirov,¹⁷ K. Trabelsi,¹⁰ S. Uehara,¹⁰ T. Uglov,¹⁷ Y. Unno,⁸
S. Uno,¹⁰ G. Varner,⁹ K. E. Varvell,⁴⁴ A. Vinokurova,^{1,38} A. Vossen,¹² C. H. Wang,³² M.-Z. Wang,³³
P. Wang,¹⁴ M. Watanabe,³⁶ Y. Watanabe,¹⁹ R. Wedd,²⁸ E. Won,²² Y. Yamashita,³⁵ C. Z. Yuan,¹⁴
Z. P. Zhang,⁴¹ V. Zhilich,^{1,38} P. Zhou,⁵⁴ V. Zhulanov,^{1,38} T. Zivko,¹⁸ A. Zupanc,²⁰ and O. Zyukova,^{1,38}

(The Belle Collaboration)

¹*Budker Institute of Nuclear Physics, Novosibirsk*

²*Faculty of Mathematics and Physics, Charles University, Prague*

³*Chiba University, Chiba*

⁴*University of Cincinnati, Cincinnati, Ohio 45221*

⁵*Justus-Liebig-Universität Gießen, Gießen*

⁶*The Graduate University for Advanced Studies, Hayama*

⁷*Gyeongsang National University, Chinju*

⁸*Hanyang University, Seoul*

⁹*University of Hawaii, Honolulu, Hawaii 96822*

¹⁰*High Energy Accelerator Research Organization (KEK), Tsukuba*

¹¹*Hiroshima Institute of Technology, Hiroshima*

¹²*University of Illinois at Urbana-Champaign, Urbana, Illinois 61801*

¹³*Indian Institute of Technology Guwahati, Guwahati*

¹⁴*Institute of High Energy Physics, Chinese Academy of Sciences, Beijing*

¹⁵*Institute of High Energy Physics, Vienna*

¹⁶*Institute of High Energy Physics, Protvino*

¹⁷*Institute for Theoretical and Experimental Physics, Moscow*

¹⁸*J. Stefan Institute, Ljubljana*

¹⁹*Kanagawa University, Yokohama*

²⁰*Institut für Experimentelle Kernphysik, Karlsruher Institut für Technologie, Karlsruhe*

²¹*Korea Institute of Science and Technology Information, Daejeon*

²²*Korea University, Seoul*

²³*Kyungpook National University, Taegu*

²⁴*École Polytechnique Fédérale de Lausanne (EPFL), Lausanne*

²⁵*Faculty of Mathematics and Physics, University of Ljubljana, Ljubljana*

²⁶*University of Maribor, Maribor*

²⁷*Max-Planck-Institut für Physik, München*

²⁸*University of Melbourne, School of Physics, Victoria 3010*

²⁹*Nagoya University, Nagoya*

³⁰*Nara Women's University, Nara*

³¹*National Central University, Chung-li*

³²*National United University, Miao Li*

³³Department of Physics, National Taiwan University, Taipei

³⁴H. Niewodniczanski Institute of Nuclear Physics, Krakow

³⁵Nippon Dental University, Niigata

³⁶Niigata University, Niigata

³⁷University of Nova Gorica, Nova Gorica

³⁸Novosibirsk State University, Novosibirsk

³⁹Osaka City University, Osaka

⁴⁰Panjab University, Chandigarh

⁴¹University of Science and Technology of China, Hefei

⁴²Seoul National University, Seoul

⁴³Sungkyunkwan University, Suwon

⁴⁴School of Physics, University of Sydney, NSW 2006

⁴⁵Tata Institute of Fundamental Research, Mumbai

⁴⁶Excellence Cluster Universe, Technische Universität München, Garching

⁴⁷Toho University, Funabashi

⁴⁸Tohoku Gakuin University, Tagajo

⁴⁹Tohoku University, Sendai

⁵⁰Department of Physics, University of Tokyo, Tokyo

⁵¹Tokyo Metropolitan University, Tokyo

⁵²Tokyo University of Agriculture and Technology, Tokyo

⁵³CNP, Virginia Polytechnic Institute and State University, Blacksburg, Virginia 24061

⁵⁴Wayne State University, Detroit, Michigan 48202

⁵⁵Yonsei University, Seoul

We report a measurement of exclusive $e^+e^- \rightarrow D_s^{(*)+} D_s^{(*)-}$ cross sections as a function of center-of-mass energy near $D_s^{(*)+} D_s^{(*)-}$ threshold with initial-state radiation. The analysis is based on a data sample collected with the Belle detector with an integrated luminosity of 967 fb^{-1} .

PACS numbers: 13.66.Bc, 13.87.Fh, 14.40.Lb

Recently a number of measurements of exclusive cross sections for e^+e^- annihilation into charmed hadron pairs above open-charm threshold were performed by the B-factory experiments using initial-state radiation (ISR). These include Belle measurements [1] of e^+e^- cross sections for the $D\bar{D}$ ($D = D^0$ or D^+), D^+D^{*-} , $D^{*+}D^{*-}$, $D^0D^-\pi^+$, $D^0D^{*-}\pi^+$ and $\Lambda_c^+\Lambda_c^-$ final states [2–6] and BaBar measurements of the $D\bar{D}$, $D\bar{D}^*$, $D^*\bar{D}^*$ final states [7, 8], which are, in general, consistent with those of Belle. In addition, CLEO scanned the e^+e^- center of mass energy range from 3.97 to 4.26 GeV and obtained exclusive cross sections for the $D\bar{D}$, $D\bar{D}^*$, $D^*\bar{D}^*$, $D\bar{D}\pi$ and $D\bar{D}^*\pi$ final states [9]. The first measurements of the exclusive cross sections for e^+e^- annihilation into charmed strange meson pairs $D_s^{(*)+} D_s^{(*)-}$ were performed by CLEO with high accuracy but with limited maximum energy (4.26 GeV) [9] and by BaBar [10] with a 100 MeV bin size. The observed cross sections were found to be an order of magnitude smaller than those for non-strange charmed meson production.

Although the recent BES fit to the total cross section for hadron production in e^+e^- provided new parameter values for the ψ resonances [11], the available *exclusive* e^+e^- cross sections have not yet been qualitatively explained. One of the main problems is the numerous open charm thresholds in the region that influence the cross section behavior and, thus, complicate theoretical descriptions.

The Y states [12] (with masses above open charm threshold and quantum numbers $J^{PC} = 1^{--}$), which do

not exhibit strong decays to any of the measured open charm final states and have remain unexplained since their discovery more than five years, provide additional motivation to pursue all possible experimental information about the decomposition of charmed particle production in the charm-threshold region.

Here we report a measurement of exclusive $e^+e^- \rightarrow D_s^{(*)+} D_s^{(*)-}$ cross sections as a function of center-of-mass energy from the $D_s^{(*)+} D_s^{(*)-}$ thresholds to 5.0 GeV, continuing our studies of the exclusive open charm production in this mass range. The analysis is based on a study of events with ISR photons in a data sample collected with the Belle detector at the $\Upsilon(nS)$ ($n = 1, \dots, 5$) resonances and nearby continuum with an integrated luminosity of 967 fb^{-1} at the KEKB asymmetric-energy e^+e^- collider.

We follow the full reconstruction method that was previously used for the measurements of the e^+e^- cross sections to $D\bar{D}$, $D^0D^-\pi^+$ and $D^0D^{*-}\pi^+$ final states [2, 4, 5]. We select $e^+e^- \rightarrow D_s^{(*)+} D_s^{(*)-} \gamma_{\text{ISR}}$ signal events in which the $D_s^{(*)+}$ and $D_s^{(*)-}$ mesons are fully reconstructed. In general, the γ_{ISR} is not required to be detected and its presence in the event is inferred from a peak at zero in the spectrum of recoil mass squared against the $D_s^{(*)+} D_s^{(*)-}$ system. The recoil mass squared is defined as:

$$M_{\text{recoil}}^2(D_s^{(*)+} D_s^{(*)-}) = (E_{\text{c.m.}} - E_{D_s^{(*)+} D_s^{(*)-}})^2 - p_{D_s^{(*)+} D_s^{(*)-}}^2, \quad (1)$$

where $E_{\text{c.m.}}$ is the initial e^+e^- center-of-mass (c.m.) energy, $E_{D_s^{(*)+}D_s^{(*)-}}$ and $p_{D_s^{(*)+}D_s^{(*)-}}$ are energy and three-momentum of the $D_s^{(*)+}D_s^{(*)-}$ combination, respectively. To suppress backgrounds two cases are considered: (1) the γ_{ISR} is outside of the detector acceptance and the polar angle for the $D_s^{(*)+}D_s^{(*)-}$ combination in the c.m. frame is in the range $|\cos(\theta_{D_s^{(*)+}D_s^{(*)-}})| > 0.9$; (2) the γ_{ISR} is within the detector acceptance ($|\cos(\theta_{D_s^{(*)+}D_s^{(*)-}})| < 0.9$). In the latter case, the γ_{ISR} is required to be detected and the mass of the $D_s^{(*)+}D_s^{(*)-}\gamma_{\text{ISR}}$ combination should be greater than $(E_{\text{c.m.}} - 0.5 \text{ GeV})$. To suppress backgrounds from $e^+e^- \rightarrow D_s^{(*)+}D_s^{(*)-}(n)(\pi^+\pi^-)\gamma_{\text{ISR}}, (n > 0)$ processes, we exclude events that contain additional charged tracks that were not used in the $D_s^{(*)+}$ and the $D_s^{(*)-}$ reconstruction.

All charged tracks are required to originate from the vicinity of the interaction point (IP); we impose the requirements $|dr| < 1 \text{ cm}$ and $|dz| < 4 \text{ cm}$, where dr and dz are the impact parameters perpendicular to and along the beam direction with respect to the IP, respectively. Charged kaons are required to have a ratio of particle identification likelihood, $\mathcal{P}_K = \mathcal{L}_K/(\mathcal{L}_K + \mathcal{L}_\pi) > 0.6$ [13]. No identification requirements are applied for pion candidates.

K_S^0 candidates are reconstructed from $\pi^+\pi^-$ pairs with an invariant mass within $10 \text{ MeV}/c^2$ of the K_S^0 mass. The distance between the two pion tracks at the K_S^0 vertex must be less than 1 cm , the transverse flight distance from the interaction point is required to be greater than 0.1 cm , and the angle between the K_S^0 momentum direction and the flight direction in the $x-y$ plane should be smaller than 0.1 rad .

Photons are reconstructed in the electromagnetic calorimeter as showers with energies greater than 50 MeV that are not associated with charged tracks. Pairs of photons are combined to form π^0 candidates. If the mass of a $\gamma\gamma$ pair lies within $15 \text{ MeV}/c^2$ of the π^0 mass, the pair is fitted with a π^0 mass constraint and considered as a π^0 candidate. ISR photon candidates are required to have energies greater than 2.5 GeV . Photon candidates used in η , η' and D_s^{*+} reconstruction are required to have energies greater than 100 MeV .

η candidates are reconstructed using $\pi^+\pi^-\pi^0$ ($\pm 10 \text{ MeV}/c^2$ mass window) and $\gamma\gamma$ ($\pm 20 \text{ MeV}/c^2$ mass window) decay modes ($\sim 2.5\sigma$ in each case). η' candidates are reconstructed using $\eta\pi^+\pi^-$ ($\pm 10 \text{ MeV}/c^2$ mass window) and $\gamma\pi^+\pi^-$ ($\pm 15 \text{ MeV}/c^2$ mass window) decay modes ($\sim 2.0\sigma$ in each case). A mass- and vertex-constrained fit is applied to η and η' candidates.

D_s^+ candidates are reconstructed using six decay modes: $K_S^0K^+$, $K^-K^+\pi^+$, $K^-K^+\pi^+\pi^0$, $K_S^0K^-\pi^+\pi^+$, $\eta\pi^+$ and $\eta'\pi^+$. Before calculation of the D_s^+ candidate mass, a vertex fit to a common vertex is performed for tracks that form the D_s^+ candidate. A $\pm 15 \text{ MeV}/c^2$ mass signal window is used for all modes ($\sim 3\sigma$ in each case). To improve the momentum resolution of D_s^+ meson can-

didates, the tracks from the D_s^+ candidate are fitted to a common vertex with a mass D_s^+ mass constraint. D_s^{*+} candidates are reconstructed using the $D_s^+\gamma$ decay mode. A $\pm 15 \text{ MeV}/c^2$ mass window is used ($\sim 2.5\sigma$). A mass-constrained fit is also applied to D_s^{*+} candidates.

The D_s^+ and D_s^{*+} sidebands used for background studies are four times as large as the signal region and are divided into windows of the same width as that of the signal. To avoid signal over-subtraction, the selected sidebands are shifted by $30 \text{ MeV}/c^2$ from the signal region. The $D_s(D_s^*)$ candidates from these sidebands are refitted to the central mass value of each window.

The $M_{\text{recoil}}^2(D_s^+D_s^-)$ distribution for $M_{D_s^+D_s^-} < 5.0 \text{ GeV}/c^2$ after all the requirements described above is shown in Fig. 1 a). A clear peak corresponding to the $e^+e^- \rightarrow D_s^+D_s^-\gamma_{\text{ISR}}$ process is evident near zero recoil mass. The shoulder at positive values is mainly due to $e^+e^- \rightarrow D_s^+D_s^{*-}\gamma_{\text{ISR}}$ background. We define the signal region with an asymmetric requirement $-0.7(\text{GeV}/c^2)^2 < M_{\text{recoil}}^2(D_s^+D_s^-) < 0.4(\text{GeV}/c^2)^2$ to suppress event this background. The polar angle distribution of the $D_s^+D_s^-$ combinations and the mass spectrum of the $D_s^+D_s^-\gamma_{\text{ISR}}$ combinations (after subtraction of $E_{\text{c.m.}}$) in case (2), after $M_{\text{recoil}}^2(D_s^+D_s^-)$ requirement, are shown in Figs. 1 b,c). These distributions are in agreement with a MC simulation and are typical of ISR production. The $M_{D_s^+D_s^-}$ spectrum with all the requirements applied is shown in Fig. 1 d). A clear peak is seen at threshold near the $\psi(4040)$ mass.

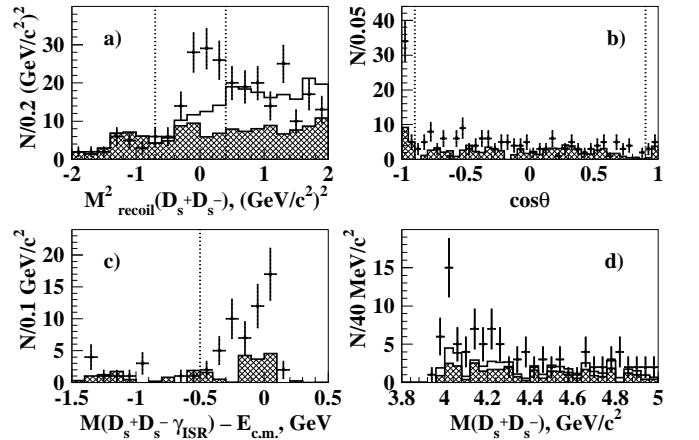


FIG. 1: a) The distribution of $M_{\text{recoil}}^2(D_s^+D_s^-)$ for $M_{D_s^+D_s^-} < 5.0 \text{ GeV}/c^2$ after all the requirements are applied. b) The polar angle distribution of the $D_s^+D_s^-$ combinations. c) The mass spectrum of the $D_s^+D_s^-\gamma_{\text{ISR}}$ combinations after subtraction of $E_{\text{c.m.}}$ energy in case (2). d) The $M_{D_s^+D_s^-}$ spectrum after all the requirements applied. Cross-hatched histograms show the normalized $M_{D_s^+}$ and $M_{D_s^-}$ sideband contributions. Feed down from the $D_s^+D_s^{*-}$ final state is shown by the open histograms. The signal windows are shown by vertical dashed lines.

The $M_{\text{recoil}}^2(D_s^+D_s^{*-})$ distribution for $M_{D_s^+D_s^{*-}} < 5.0 \text{ GeV}/c^2$ after all the requirements are applied is shown

in Fig. 2a). A clear peak corresponding to $e^+e^- \rightarrow D_s^+ D_s^{*-} \gamma_{\text{ISR}}$ signal process is again evident around zero. We define the signal region for $M_{\text{recoil}}^2(D_s^+ D_s^{*-})$ by a requirement $\pm 0.7 (\text{GeV}/c^2)^2$ around zero. The polar angle distribution of the $D_s^+ D_s^{*-}$ combinations and the mass spectrum of $D_s^+ D_s^{*-} \gamma_{\text{ISR}}$ combinations (after subtraction of the $E_{\text{c.m.}}$ energy) in case (2) after the requirement on $M_{\text{recoil}}^2(D_s^+ D_s^{*-})$ is applied are shown in Figs. 2 b, c). The $M_{D_s^+ D_s^{*-}}$ spectrum after all the requirements are applied is shown in Fig. 2d). Two clear peaks are seen at the $\psi(4160)$ and the $\psi(4415)$ masses.

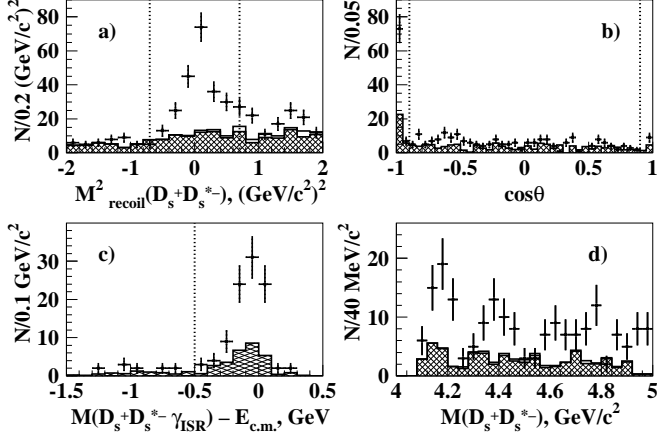


FIG. 2: a) The distribution of the $M_{\text{recoil}}^2(D_s^+ D_s^{*-})$ for $M_{D_s^+ D_s^{*-}} < 5.0 \text{ GeV}/c^2$ after all the requirements applied. b) The polar angle distribution of the $D_s^+ D_s^{*-}$ combinations. c) The mass spectrum of the $D_s^+ D_s^{*-} \gamma_{\text{ISR}}$ combinations after subtraction of $E_{\text{c.m.}}$ in case (2). d) The obtained $M_{D_s^+ D_s^{*-}}$ spectrum. Cross-hatched histograms show the normalized $M_{D_s^+}$ and $M_{D_s^{*-}}$ sidebands contributions. The small contamination from the $D_s^{*+} D_s^{*-}$ final state is shown by the open histograms. The signal windows are shown by vertical dashed lines.

The $M_{\text{recoil}}^2(D_s^{*+} D_s^{*-})$ distribution for $M_{D_s^{*+} D_s^{*-}} < 5.0 \text{ GeV}/c^2$ after all the requirements applied is shown in Fig. 3a). A peak corresponding to $e^+e^- \rightarrow D_s^{*+} D_s^{*-} \gamma_{\text{ISR}}$ is again evident around zero recoil mass. We define the signal region for $M_{\text{recoil}}^2(D_s^{*+} D_s^{*-})$ by a requirement $\pm 0.7 (\text{GeV}/c^2)^2$ around zero recoil mass. The polar angle distribution of the $D_s^{*+} D_s^{*-}$ combinations and the mass spectrum of the $D_s^{*+} D_s^{*-} \gamma_{\text{ISR}}$ combinations (after subtraction of $E_{\text{c.m.}}$) that survive the $M_{\text{recoil}}^2(D_s^{*+} D_s^{*-})$ requirement in case (2) are shown in Figs. 3 b, c). The full $M_{D_s^{*+} D_s^{*-}}$ spectrum after all the requirements are applied is shown in Fig. 3d). With such limited statistics no structure are evident.

The contribution of multiple entries after all the requirements is found to be $\sim 6\%$, $\sim 22\%$, $\sim 23\%$, for the $D_s^+ D_s^-$, $D_s^+ D_s^{*-}$ and the $D_s^{*+} D_s^{*-}$ final states, respectively. In such cases, only one $D_s^{(*)+} D_s^{(*)-}$ combination per event, that with the minimum value of $\chi_{\text{tot}}^2 = \chi_{M(D_s^+)}^2 + \chi_{M(D_s^-)}^2 + (\chi_{M(D_s^{*+})}^2 + \chi_{M(D_s^{*-})}^2)$, is

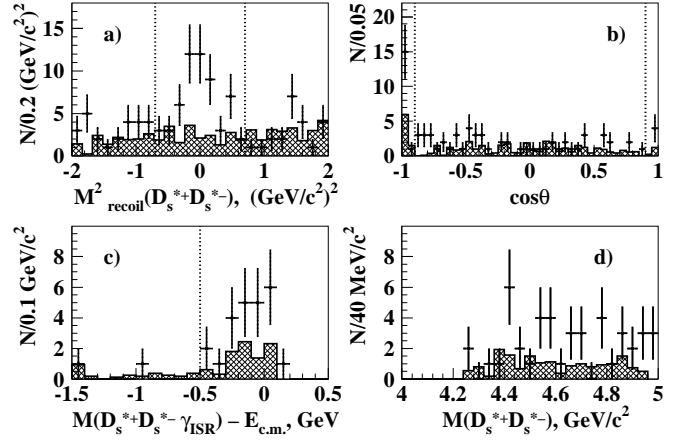


FIG. 3: a) The distributions of the $M_{\text{recoil}}^2(D_s^{*+} D_s^{*-})$ for $M_{D_s^{*+} D_s^{*-}} < 5.0 \text{ GeV}/c^2$ after all the requirements applied. b) The polar angle distribution of the $D_s^{*+} D_s^{*-}$ combinations. c) The mass spectrum of the $D_s^{*+} D_s^{*-} \gamma_{\text{ISR}}$ combinations after subtraction of $E_{\text{c.m.}}$ in case (2). d) The $M_{D_s^{*+} D_s^{*-}}$ spectrum after all the requirements applied. Cross-hatched histograms show the normalized $M_{D_s^{*+}}$ and $M_{D_s^{*-}}$ sidebands contributions. The signal windows are shown by vertical dashed lines.

used, where $\chi_{M(D_s^+)}^2$, $\chi_{M(D_s^-)}^2$, $\chi_{M(D_s^{*+})}^2$ and $\chi_{M(D_s^{*-})}^2$ correspond to the mass fits for the D_s^+ , D_s^- , D_s^{*+} and the D_s^{*-} candidates.

The following sources of background are considered: (1) combinatorial background under the $D_s^{(*)+}(D_s^{*-})$ peak combined with a correctly reconstructed $D_s^{(*)-}(D_s^{*+})$ from the signal or other processes; (2) both the $D_s^{(*)+}$ and the $D_s^{(*)-}$ are combinatorial; (3) for the $D_s^+ D_s^-$ final state: reflections from the $e^+e^- \rightarrow D_s^+ D_s^- \gamma_{\text{ISR}}$ and $e^+e^- \rightarrow D_s^{*+} D_s^{*-} \gamma_{\text{ISR}}$ processes followed by $D_s^* \rightarrow D_s \gamma$, where the low momentum γ is not reconstructed; for the $D_s^+ D_s^{*-}$ final state: reflection from the $e^+e^- \rightarrow D_s^{*+} D_s^{*-} \gamma_{\text{ISR}}$ process followed by $D_s^* \rightarrow D_s \gamma$, where the low momentum γ is not reconstructed; (4) reflection from the $e^+e^- \rightarrow D_s^{(*)+} D_s^{(*)-} \pi_{\text{miss}}^0 \gamma_{\text{ISR}}$ processes, where the π_{miss}^0 is not reconstructed. (5) the contribution of $e^+e^- \rightarrow D_s^{(*)+} D_s^{(*)-} \pi^0$, when an energetic π^0 is misidentified as a single γ_{ISR} .

The contribution from background (1) is extracted using the $D_s^{(*)-}$ and $D_s^{(*)+}$ sidebands. Background (2) is present in both the $M_{D_s^{(*)+}}$ and $M_{D_s^{(*)-}}$ sidebands and is, thus, subtracted twice. To account for this over-subtraction we use a double sideband region, when events are selected from both the $M_{D_s^{(*)+}}$ and the $M_{D_s^{(*)-}}$ sidebands. The contributions from the combinatorial backgrounds (1-2) are shown in Figs. 1 d) and 2 d) as cross-hatched histograms.

Backgrounds (3-4) are suppressed by the tight requirement on $M_{\text{recoil}}^2(D_s^{(*)+} D_s^{(*)-})$. The remaining background (3) for the $D_s^+ D_s^{*-}$ final state is estimated using a MC simulation of the $e^+e^- \rightarrow D_s^{*+} D_s^{*-} \gamma_{\text{ISR}}$ pro-

cess. To reproduce the shape of the $D_s^+ D_s^{*-}$ mass spectrum we use the initial measurement of the $D_s^{*+} D_s^{*-}$ mass spectrum. The remainder of background (3) for the $D_s^+ D_s^-$ final state is estimated using a MC simulation of the $e^+ e^- \rightarrow D_s^+ D_s^{*-} \gamma_{\text{ISR}}$ and $e^+ e^- \rightarrow D_s^{*+} D_s^{*-} \gamma_{\text{ISR}}$ processes. To reproduce the shape of the $D_s^+ D_s^-$ mass spectrum we use the initial measurement of the $D_s^{*+} D_s^{*-}$ mass spectrum and the first iteration of the $D_s^+ D_s^{*-}$ mass spectrum. The contributions from background (3) for the $D_s^+ D_s^-$ and the $D_s^+ D_s^{*-}$ final states are shown in Figs. 1 a), 1 d) and Figs. 2 a), 2 d) as open histograms. Uncertainties in these estimates are included in the systematic errors.

To estimate the contribution from background (4), we study the $e^+ e^- \rightarrow D_s^{(*)+} D_s^{(*)-} \pi^0 \gamma_{\text{ISR}}$ processes using fully reconstructed final states. From a MC study we estimate the fraction of reconstructed events for the cases where the π^0 is not detected. After the application of the requirement on $M_{\text{recoil}}^2(D_s^{(*)+} D_s^{(*)-})$ this contribution is found to be less than 0.5% and negligibly small; uncertainties in this estimate are included in the systematic errors.

The contribution from background (5), in which an energetic π^0 is misidentified as the γ_{ISR} candidate, is determined from the data using fully reconstructed $e^+ e^- \rightarrow D_s^{(*)+} D_s^{(*)-} \pi^0$ events. Only three events with $M_{D_s^+ D_s^-} < 5.0 \text{ GeV}/c^2$ and $M_{D_s^+ D_s^-} \pi^0 - E_{\text{c.m.}} > 0.5 \text{ GeV}$ are found in the data. Assuming a uniform π^0 polar angle distribution, this background contribution in the $|\cos(\theta_{D_s^+ D_s^-})| > 0.9$ signal sub-sample (case 1) is 3 events/ $9\epsilon_{\pi^0} \sim 0.6$ events in the whole $M_{D_s^+ D_s^-}$ mass range, where ϵ_{π^0} is

the π^0 reconstruction efficiency. For the $D_s^+ D_s^{*-}$ and the $D_s^{*+} D_s^{*-}$ final states the expected backgrounds are ~ 0.6 events and 0 events in the whole $M_{D_s^+ D_s^{*-}}$ and $M_{D_s^{*+} D_s^{*-}}$ mass ranges. The probability of $\pi^0 \rightarrow \gamma\gamma$ misidentification due to asymmetric $\pi^0 \rightarrow \gamma\gamma$ decays is also estimated to be small. Thus the contribution from background (5) is found to be negligibly small; uncertainties in these estimates are included in the systematic error.

The $e^+ e^- \rightarrow D_s^{(*)+} D_s^{(*)-}$ cross sections are extracted from the background subtracted $D_s^{(*)+} D_s^{(*)-}$ mass distributions

$$\sigma(e^+ e^- \rightarrow D_s^{(*)+} D_s^{(*)-}) = \frac{dN/dm}{\eta_{\text{tot}} dL/dm}, \quad (2)$$

where $m \equiv M_{D_s^{(*)+} D_s^{(*)-}}$, dN/dm is the obtained mass spectrum, η_{tot} is the total efficiency and the factor dL/dm is the differential ISR luminosity [15]. The total efficiencies determined by the MC simulation grow quadratically with energy from 0.015%, 0.010%, 0.005% near threshold to 0.045%, 0.025%, 0.011% at $5.0 \text{ GeV}/c^2$ for the $D_s^+ D_s^-$, $D_s^+ D_s^{*-}$ and the $D_s^{*+} D_s^{*-}$ final states, respectively. The resulting $e^+ e^- \rightarrow D_s^{(*)+} D_s^{(*)-}$ exclusive cross sections averaged over the bin width are shown in Fig. 4. Since the bin width is much larger than the $M_{D_s^{(*)+} D_s^{(*)-}}$ resolution, which varies from $\sim 2 \text{ MeV}/c^2$ around threshold to $\sim 6 \text{ MeV}/c^2$ at $M_{D_s^{(*)+} D_s^{(*)-}} = 5.0 \text{ GeV}/c^2$, no correction for resolution is applied. The next-to-leading order radiative corrections are taken into account by the dL/dm formula. The next-to-next-to-leading order corrections are included in the systematics.

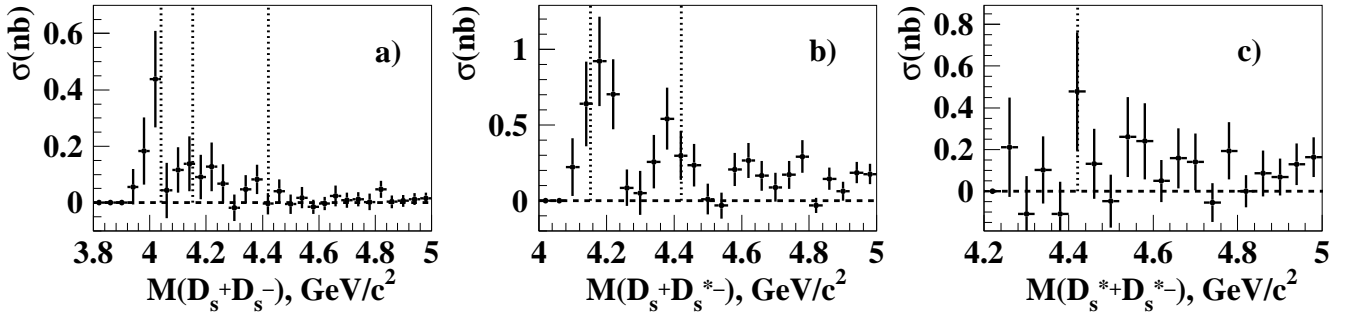


FIG. 4: The cross section averaged over the bin width for a) the $e^+ e^- \rightarrow D_s^+ D_s^-$ process; b) the $e^+ e^- \rightarrow D_s^+ D_s^{*-} + \text{c.c.}$ process; c) the $e^+ e^- \rightarrow D_s^{*+} D_s^{*-}$ process. Error bars show statistical uncertainties only. There is a common systematic uncertainty for all measurements, 11% for $D_s^+ D_s^-$, 17% for $D_s^+ D_s^{*-}$ and 31% for $D_s^{*+} D_s^{*-}$. This uncertainty is described in the text. The dotted lines show masses of the $\psi(4040)$, $\psi(4160)$ and $\psi(4415)$ states [14].

The R ratio, defined as $R = \sigma(e^+ e^- \rightarrow \text{hadrons})/\sigma(e^+ e^- \rightarrow \mu^+ \mu^-)$, where $\sigma(e^+ e^- \rightarrow \mu^+ \mu^-) = 4\pi\alpha^2/3s$, for the sum of the exclusive $e^+ e^- \rightarrow D_s^{(*)+} D_s^{(*)-}$ cross sections is shown in Fig. 5.

The systematic errors for the $\sigma(e^+ e^- \rightarrow D_s^{(*)+} D_s^{(*)-})$ measurements are summarized in Table I. The systematic errors associated with the background (1–2) subtraction are estimated from the uncertainty in the scaling fac-

tors for the sideband subtractions. This is done using fits to the $M_{D_s^{(*)+}}$ and $M_{D_s^{(*)-}}$ distributions in the data with different signal and background parameterizations and are found to be 3%, 7% and 24% for the $D_s^+ D_s^-$, $D_s^+ D_s^{*-}$ and the $D_s^{*+} D_s^{*-}$ final states, respectively. Uncertainties in the contribution from background (3) are estimated to be 2% for the $D_s^+ D_s^-$ final state and smaller than 1% for the $D_s^+ D_s^{*-}$ final state. Uncertainties in the backgrounds (4–5) are estimated conservatively to be smaller

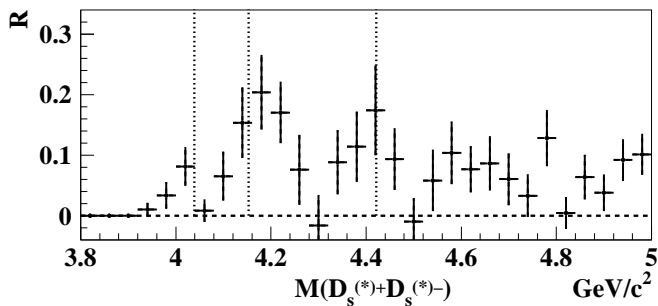


FIG. 5: The R ratio for the sum of the $D_s^+ D_s^-$, $D_s^+ D_s^{*-}$ and the $D_s^{*+} D_s^{*-}$ final states. The vertical dotted lines show the masses of the $\psi(4040)$, $\psi(4160)$ and $\psi(4415)$ states [14]. Error bars show statistical uncertainties only.

TABLE I: Contributions to the systematic error on the cross sections.

Source	$D_s^+ D_s^-$	$D_s^+ D_s^{*-}$	$D_s^{*+} D_s^{*-}$
Background subtraction	$\pm 4\%$	$\pm 7\%$	$\pm 24\%$
Cross section calculation	$\pm 7\%$	$\pm 11\%$	$\pm 12\%$
$\mathcal{B}(D_s^{(*)})$	$\pm 5\%$	$\pm 5\%$	$\pm 5\%$
Reconstruction	$\pm 6\%$	$\pm 10\%$	$\pm 16\%$
Kaon identification	$\pm 2\%$	$\pm 2\%$	$\pm 2\%$
Total	$\pm 11\%$	$\pm 17\%$	$\pm 31\%$

than 1% of the signal for all final states. The systematic errors ascribed to the cross section calculation include an error on the differential ISR luminosity (2%) and statistical errors of the MC simulation for the total efficiency calculations. In the case of the $D_s^+ D_s^{*-}$ state there is an additional uncertainty due to the unknown helicity distribution, estimated following a procedure similar to that used in Ref [3]. Another source of systematic error comes from the uncertainties in track and photon reconstruction efficiencies (1% per track, 1.5% per photon and 7% per soft photon). Other contributions include the uncertainty in the identification efficiency and the absolute D_s^+ and D_s^{*+} branching fractions [14]. The total systematic uncertainties are 11%, 17% and 31% for the $D_s^+ D_s^-$, $D_s^+ D_s^{*-}$ and the $D_s^{*+} D_s^{*-}$ final states, respectively.

In summary, we report the measurement of the $e^+e^- \rightarrow D_s^{(*)+} D_s^{(*)-}$ exclusive cross sections over the center-of-mass energy range from the $D_s^{(*)+} D_s^{(*)-}$ thresholds to 5.0 GeV. A clear peak at threshold around the $\psi(4040)$ mass is seen in the $e^+e^- \rightarrow D_s^+ D_s^-$ cross section. In the $e^+e^- \rightarrow D_s^+ D_s^{*-}$ cross section two peaks are evident around the $\psi(4160)$ and the $\psi(4415)$ masses.

The limited statistics do not reveal any structures in the $e^+e^- \rightarrow D_s^{*+} D_s^{*-}$ cross section. The obtained R ratio for the sum of $e^+e^- \rightarrow D_s^{(*)+} D_s^{(*)-}$ cross sections has a rich structure including peaks around the $\psi(4040)$, $\psi(4160)$ and the $\psi(4415)$ masses. Both the $e^+e^- \rightarrow D_s^+ D_s^{*-}$ cross section and the R ratio exhibit an obvious dip near the $Y(4260)$ mass, similar to what is seen in $e^+e^- \rightarrow D^* \bar{D}^*$ and in the total cross section for charm production. The obtained cross sections are consistent within errors with those from BaBar [10]. The CLEO exclusive cross sections [9] are not directly comparable to those from Belle as they are not radiatively corrected, but generally seem to reflect consistency.

In this study we do not perform a fit to the obtained $e^+e^- \rightarrow D_s^{(*)+} D_s^{(*)-}$ cross sections. The numerous open charm thresholds in this region complicate the cross sections behavior and coupled-channel modifications to the description of any particular final state require one to take into account all other final states contributing to the total cross section for charm production.

We thank the KEKB group for the excellent operation of the accelerator, the KEK cryogenics group for the efficient operation of the solenoid, and the KEK computer group and the National Institute of Informatics for valuable computing and SINET3 network support. We acknowledge support from the Ministry of Education, Culture, Sports, Science, and Technology (MEXT) of Japan, the Japan Society for the Promotion of Science (JSPS), and the Tau-Lepton Physics Research Center of Nagoya University; the Australian Research Council and the Australian Department of Industry, Innovation, Science and Research; the National Natural Science Foundation of China under contract No. 10575109, 10775142, 10875115 and 10825524; the Ministry of Education, Youth and Sports of the Czech Republic under contract No. LA10033 and MSM0021620859; the Department of Science and Technology of India; the BK21 and WCU program of the Ministry Education Science and Technology, National Research Foundation of Korea, and NSDC of the Korea Institute of Science and Technology Information; the Polish Ministry of Science and Higher Education; the Ministry of Education and Science of the Russian Federation and the Russian Federal Agency for Atomic Energy; the Slovenian Research Agency; the Swiss National Science Foundation; the National Science Council and the Ministry of Education of Taiwan; and the U.S. Department of Energy. This work is supported by a Grant-in-Aid from MEXT for Science Research in a Priority Area (“New Development of Flavor Physics”), and from JSPS for Creative Scientific Research (“Evolution of Tau-lepton Physics”).

[1] Charge-conjugate modes are included throughout this paper.

[2] G. Pakhlova *et al.* (Belle Collab.), Phys. Rev. D **77**, 011103 (2008).

- [3] G. Pakhlova *et al.* (Belle Collab.), Phys. Rev. Lett. **98**, 092001 (2007).
- [4] G. Pakhlova *et al.* (Belle Collab.), Phys. Rev. Lett. **100**, 062001 (2008).
- [5] G. Pakhlova *et al.* (Belle Collab.), Phys. Rev. D **80**, 091101 (2009).
- [6] G. Pakhlova *et al.* (Belle Collab.), Phys. Rev. Lett. **101**, 172001 (2008).
- [7] B. Aubert *et al.* (BaBar Collab.), Phys. Rev. D **76**, 111105 (2007).
- [8] B. Aubert *et al.* (BaBar Collab.), Phys. Rev. D **79**, 092001 (2009).
- [9] D. Cronin-Hennessy *et al.* (CLEO Collab.), Phys. Rev. D **80**, 072001 (2009).
- [10] P. del Amo Sanchez *et al.* (BaBar Collab.), Phys. Rev. D **82**, 052004 (2010).
- [11] M. Ablikim *et al.* (BES Collab.), Phys. Lett. B **660**, 315 (2008).
- [12] B. Aubert *et al.* (BaBar Collab.), Phys. Rev. Lett. **95**, 142001 (2005); T. E. Coan *et al.* (CLEO Collab.), Phys. Rev. Lett. **96**, 162003 (2006); Q. He *et al.* (CLEO Collab.), Phys. Rev. D **74**, 091104 (2006); C. Z. Yuan *et al.* (Belle Collab.), Phys. Rev. Lett. **99**, 182004 (2007); B. Aubert *et al.* (BaBar Collab.), arXiv:0808.1543 [hep-ex], (2008); B. Aubert *et al.* (BaBar Collab.), Phys. Rev. Lett. **98**, 212001 (2007); X. L. Wang *et al.* (Belle Collab.), Phys. Rev. Lett. **99**, 142002 (2007); Z. Q. Liu, X. S. Qin and C. Z. Yuan, Phys. Rev. D **78**, 014032 (2008).
- [13] E. Nakano, Nucl. Instrum. Meth., A **494**, 402 (2002).
- [14] K. Nakamura *et al.* (Particle Data Group), J. Phys. G **37**, 075021 (2010).
- [15] E. A. Kuraev and V. S. Fadin, Sov. J. Nucl. Phys. **41**, 466 (1985) [Yad. Fiz **41**, 733 (1985)].

Measurement of $e^+e^- \rightarrow D_s^{(*)+} D_s^{(*)-}$ cross sections near threshold using initial-state radiation

G. Pakhlova,¹⁷ I. Adachi,¹⁰ H. Aihara,⁵⁰ K. Arinstein,^{1,38} T. Aushev,^{24,17} T. Aziz,⁴⁵ A. M. Bakich,⁴⁴
V. Balagura,¹⁷ E. Barberio,²⁸ A. Bay,²⁴ K. Belous,¹⁶ V. Bhardwaj,⁴⁰ B. Bhuyan,¹³ A. Bondar,^{1,38}
A. Bozek,³⁴ M. Bračko,^{26,18} T. E. Browder,⁹ A. Chen,³¹ P. Chen,³³ B. G. Cheon,⁸ R. Chistov,¹⁷ I.-S. Cho,⁵⁵
K. Cho,²¹ K.-S. Choi,⁵⁵ S.-K. Choi,⁷ Y. Choi,⁴³ J. Dalseno,^{27,46} M. Danilov,¹⁷ Z. Doležal,² A. Drutskoy,⁴
S. Eidelman,^{1,38} D. Epifanov,^{1,38} N. Gabyshev,^{1,38} A. Garmash,^{1,38} B. Golob,^{25,18} H. Ha,²² J. Haba,¹⁰
K. Hayasaka,²⁹ H. Hayashii,³⁰ Y. Horii,⁴⁹ Y. Hoshi,⁴⁸ W.-S. Hou,³³ H. J. Hyun,²³ T. Iijima,²⁹ K. Inami,²⁹
R. Itoh,¹⁰ M. Iwabuchi,⁵⁵ Y. Iwasaki,¹⁰ N. J. Joshi,⁴⁵ T. Julius,²⁸ J. H. Kang,⁵⁵ P. Kapusta,³⁴ H. Kawai,³
T. Kawasaki,³⁶ C. Kiesling,²⁷ H. J. Kim,²³ H. O. Kim,²³ M. J. Kim,²³ S. K. Kim,⁴² Y. J. Kim,⁶ K. Kinoshita,⁴
B. R. Ko,²² S. Korpar,^{26,18} P. Krizan,^{25,18} T. Kumita,⁵¹ A. Kuzmin,^{1,38} Y.-J. Kwon,⁵⁵ S.-H. Kyeong,⁵⁵
J. S. Lange,⁵ M. J. Lee,⁴² S.-H. Lee,²² C. Liu,⁴¹ Y. Liu,³³ D. Liventsev,¹⁷ R. Louvot,²⁴ A. Matyja,³⁴ S. McOnie,⁴⁴
K. Miyabayashi,³⁰ H. Miyata,³⁶ Y. Miyazaki,²⁹ R. Mizuk,¹⁷ G. B. Mohanty,⁴⁵ T. Mori,²⁹ Y. Nagasaka,¹¹
E. Nakano,³⁹ M. Nakao,¹⁰ H. Nakazawa,³¹ S. Nishida,¹⁰ K. Nishimura,⁹ O. Nitoh,⁵² T. Nozaki,¹⁰ S. Ogawa,⁴⁷
T. Ohshima,²⁹ S. Okuno,¹⁹ S. L. Olsen,^{42,9} P. Pakhlov,¹⁷ H. Palka,³⁴ C. W. Park,⁴³ H. Park,²³ H. K. Park,²³
R. Pestotnik,¹⁸ M. Petrič,¹⁸ L. E. Piilonen,⁵³ A. Poluektov,^{1,38} M. Röhrken,²⁰ S. Ryu,⁴² H. Sahoo,⁹ K. Sakai,¹⁰
Y. Sakai,¹⁰ O. Schneider,²⁴ C. Schwanda,¹⁵ K. Senyo,²⁹ M. E. Sevir,²⁸ M. Shapkin,¹⁶ V. Shebalin,^{1,38} C. P. Shen,⁹
J.-G. Shiu,³³ B. Shwartz,^{1,38} F. Simon,^{27,46} P. Smerkol,¹⁸ Y.-S. Sohn,⁵⁵ A. Sokolov,¹⁶ E. Solovieva,¹⁷ S. Stanič,³⁷
M. Starič,¹⁸ T. Sumiyoshi,⁵¹ Y. Teramoto,³⁹ I. Tikhomirov,¹⁷ K. Trabelsi,¹⁰ S. Uehara,¹⁰ T. Uglov,¹⁷ Y. Unno,⁸
S. Uno,¹⁰ G. Varner,⁹ K. E. Varvell,⁴⁴ A. Vinokurova,^{1,38} A. Vossen,¹² C. H. Wang,³² M.-Z. Wang,³³
P. Wang,¹⁴ M. Watanabe,³⁶ Y. Watanabe,¹⁹ R. Wedd,²⁸ E. Won,²² Y. Yamashita,³⁵ C. Z. Yuan,¹⁴
Z. P. Zhang,⁴¹ V. Zhilich,^{1,38} P. Zhou,⁵⁴ V. Zhulanov,^{1,38} T. Zivko,¹⁸ A. Zupanc,²⁰ and O. Zyukova,^{1,38}

(The Belle Collaboration)

¹*Budker Institute of Nuclear Physics, Novosibirsk*

²*Faculty of Mathematics and Physics, Charles University, Prague*

³*Chiba University, Chiba*

⁴*University of Cincinnati, Cincinnati, Ohio 45221*

⁵*Justus-Liebig-Universität Gießen, Gießen*

⁶*The Graduate University for Advanced Studies, Hayama*

⁷*Gyeongsang National University, Chinju*

⁸*Hanyang University, Seoul*

⁹*University of Hawaii, Honolulu, Hawaii 96822*

¹⁰*High Energy Accelerator Research Organization (KEK), Tsukuba*

¹¹*Hiroshima Institute of Technology, Hiroshima*

¹²*University of Illinois at Urbana-Champaign, Urbana, Illinois 61801*

¹³*Indian Institute of Technology Guwahati, Guwahati*

¹⁴*Institute of High Energy Physics, Chinese Academy of Sciences, Beijing*

¹⁵*Institute of High Energy Physics, Vienna*

¹⁶*Institute of High Energy Physics, Protvino*

¹⁷*Institute for Theoretical and Experimental Physics, Moscow*

¹⁸*J. Stefan Institute, Ljubljana*

¹⁹*Kanagawa University, Yokohama*

²⁰*Institut für Experimentelle Kernphysik, Karlsruher Institut für Technologie, Karlsruhe*

²¹*Korea Institute of Science and Technology Information, Daejeon*

²²*Korea University, Seoul*

²³*Kyungpook National University, Taegu*

²⁴*École Polytechnique Fédérale de Lausanne (EPFL), Lausanne*

²⁵*Faculty of Mathematics and Physics, University of Ljubljana, Ljubljana*

²⁶*University of Maribor, Maribor*

²⁷*Max-Planck-Institut für Physik, München*

²⁸*University of Melbourne, School of Physics, Victoria 3010*

²⁹*Nagoya University, Nagoya*

³⁰*Nara Women's University, Nara*

³¹*National Central University, Chung-li*

³²*National United University, Miao Li*

³³Department of Physics, National Taiwan University, Taipei

³⁴H. Niewodniczanski Institute of Nuclear Physics, Krakow

³⁵Nippon Dental University, Niigata

³⁶Niigata University, Niigata

³⁷University of Nova Gorica, Nova Gorica

³⁸Novosibirsk State University, Novosibirsk

³⁹Osaka City University, Osaka

⁴⁰Panjab University, Chandigarh

⁴¹University of Science and Technology of China, Hefei

⁴²Seoul National University, Seoul

⁴³Sungkyunkwan University, Suwon

⁴⁴School of Physics, University of Sydney, NSW 2006

⁴⁵Tata Institute of Fundamental Research, Mumbai

⁴⁶Excellence Cluster Universe, Technische Universität München, Garching

⁴⁷Toho University, Funabashi

⁴⁸Tohoku Gakuin University, Tagajo

⁴⁹Tohoku University, Sendai

⁵⁰Department of Physics, University of Tokyo, Tokyo

⁵¹Tokyo Metropolitan University, Tokyo

⁵²Tokyo University of Agriculture and Technology, Tokyo

⁵³CNP, Virginia Polytechnic Institute and State University, Blacksburg, Virginia 24061

⁵⁴Wayne State University, Detroit, Michigan 48202

⁵⁵Yonsei University, Seoul

We report a measurement of exclusive $e^+e^- \rightarrow D_s^{(*)+} D_s^{(*)-}$ cross sections as a function of center-of-mass energy near $D_s^{(*)+} D_s^{(*)-}$ threshold with initial-state radiation. The analysis is based on a data sample collected with the Belle detector with an integrated luminosity of 967 fb^{-1} .

PACS numbers: 13.66.Bc, 13.87.Fh, 14.40.Lb

Recently a number of measurements of exclusive cross sections for e^+e^- annihilation into charmed hadron pairs above open-charm threshold were performed by the B-factory experiments using initial-state radiation (ISR). These include Belle measurements [1] of e^+e^- cross sections for the $D\bar{D}$ ($D = D^0$ or D^+), D^+D^{*-} , $D^{*+}D^{*-}$, $D^0D^-\pi^+$, $D^0D^{*-}\pi^+$ and $\Lambda_c^+\Lambda_c^-$ final states [2–6] and BaBar measurements of the $D\bar{D}$, $D\bar{D}^*$, $D^*\bar{D}^*$ final states [7, 8], which are, in general, consistent with those of Belle. In addition, CLEO scanned the e^+e^- center of mass energy range from 3.97 to 4.26 GeV and obtained exclusive cross sections for the $D\bar{D}$, $D\bar{D}^*$, $D^*\bar{D}^*$, $D\bar{D}\pi$ and $D\bar{D}^*\pi$ final states [9]. The first measurements of the exclusive cross sections for e^+e^- annihilation into *charmed strange* meson pairs $D_s^{(*)+} D_s^{(*)-}$ were performed by CLEO with high accuracy but with limited maximum energy (4.26 GeV) [9]. Recently BaBar presented $e^+e^- \rightarrow D_s^{(*)+} D_s^{(*)-}$ cross sections averaged over 100 MeV wide bins [10]. The observed cross sections were found to be an order of magnitude smaller than those for non-strange charmed meson production.

Although the recent BES fit to the total cross section for hadron production in e^+e^- provided new parameter values for the ψ resonances [11], the available *exclusive* e^+e^- cross sections have not yet been qualitatively explained. One of the main problems is the numerous open charm thresholds in the region that influence the cross section behavior and, thus, complicate theoretical descriptions.

The Y states [12] (with masses above open charm

threshold and quantum numbers $J^{PC} = 1^{--}$), which do not exhibit strong decays to any of the measured open charm final states and have remain unexplained since their discovery more than five years, provide additional motivation to pursue all possible experimental information about the decomposition of charmed particle production in the charm-threshold region.

Here we report a measurement of exclusive $e^+e^- \rightarrow D_s^{(*)+} D_s^{(*)-}$ cross sections as a function of center-of-mass energy from the $D_s^{(*)+} D_s^{(*)-}$ thresholds to 5.0 GeV, continuing our studies of the exclusive open charm production in this mass range. The analysis is based on a study of events with ISR photons in a data sample collected with the Belle detector [13] at the $\Upsilon(nS)$ ($n = 1, \dots, 5$) resonances and nearby continuum with an integrated luminosity of 967 fb^{-1} at the KEKB [14] asymmetric-energy e^+e^- collider.

We follow the full reconstruction method that was previously used for the measurements of the e^+e^- cross sections to $D\bar{D}$, $D^0D^-\pi^+$ and $D^0D^{*-}\pi^+$ final states [2, 4, 5]. We select $e^+e^- \rightarrow D_s^{(*)+} D_s^{(*)-} \gamma_{\text{ISR}}$ signal events in which the $D_s^{(*)+}$ and $D_s^{(*)-}$ mesons are fully reconstructed. ISR photon candidates are indicated by γ_{ISR} . In general, an γ_{ISR} is not required to be detected and its presence in the event is inferred from a peak at zero in the spectrum of recoil mass squared against the $D_s^{(*)+} D_s^{(*)-}$

system. The recoil mass squared is defined as:

$$M_{\text{recoil}}^2(D_s^{(*)+}D_s^{(*)-}) = (E_{\text{c.m.}} - E_{D_s^{(*)+}D_s^{(*)-}})^2 - p_{D_s^{(*)+}D_s^{(*)-}}^2, \quad (1)$$

where $E_{\text{c.m.}}$ is the initial e^+e^- center-of-mass (c.m.) energy, $E_{D_s^{(*)+}D_s^{(*)-}}$ and $p_{D_s^{(*)+}D_s^{(*)-}}$ are energy and three-momentum of the $D_s^{(*)+}D_s^{(*)-}$ combination, respectively. To suppress backgrounds two cases are considered: (1) the γ_{ISR} is outside of the detector acceptance and the polar angle for the $D_s^{(*)+}D_s^{(*)-}$ combination in the c.m. frame is in the range $|\cos(\theta_{D_s^{(*)+}D_s^{(*)-}})| > 0.9$; (2) the γ_{ISR} is within the detector acceptance ($|\cos(\theta_{D_s^{(*)+}D_s^{(*)-}})| < 0.9$). In the latter case, the γ_{ISR} is required to be detected and the mass of the $D_s^{(*)+}D_s^{(*)-}\gamma_{\text{ISR}}$ combination should to be greater than $(E_{\text{c.m.}} - 0.5 \text{ GeV})$. To suppress backgrounds from $e^+e^- \rightarrow D_s^{(*)+}D_s^{(*)-}(m)(\pi^+\pi^-)\gamma_{\text{ISR}}$, ($m = 1, 2, \dots$) processes, we exclude events that contain additional charged tracks that were not used in the $D_s^{(*)+}$ and the $D_s^{(*)-}$ reconstruction.

All charged tracks are required to originate from the vicinity of the interaction point (IP); we impose the requirements $|dr| < 1 \text{ cm}$ and $|dz| < 4 \text{ cm}$, where dr and dz are the impact parameters perpendicular to and along the beam direction with respect to the IP, respectively. Charged kaons are required to have a ratio of particle identification likelihood, $\mathcal{P}_K = \mathcal{L}_K/(\mathcal{L}_K + \mathcal{L}_\pi) > 0.6$ [15]. No identification requirements are applied for pion candidates.

K_S^0 candidates are reconstructed from $\pi^+\pi^-$ pairs with an invariant mass within $10 \text{ MeV}/c^2$ of the K_S^0 mass. The distance between the two pion tracks at the K_S^0 vertex must be less than 1 cm , the transverse flight distance from the interaction point is required to be greater than 0.1 cm , and the angle between the K_S^0 momentum direction and the flight direction in the $x-y$ plane should be smaller than 0.1 rad .

Photons are reconstructed in the electromagnetic calorimeter as showers with energies greater than 50 MeV that are not associated with charged tracks. Pairs of photons are combined to form π^0 candidates. If the mass of a $\gamma\gamma$ pair lies within $15 \text{ MeV}/c^2$ of the π^0 mass, the pair is fitted with a π^0 mass constraint and considered as a π^0 candidate. ISR photon candidates are required to have energies greater than 2.5 GeV . Photon candidates used in η , η' and D_s^{*+} reconstruction are required to have energies greater than 100 MeV .

η candidates are reconstructed using $\pi^+\pi^-\pi^0$ ($\pm 10 \text{ MeV}/c^2$ mass window) and $\gamma\gamma$ ($\pm 20 \text{ MeV}/c^2$ mass window) decay modes ($\sim 2.5\sigma$ in each case). η' candidates are reconstructed using $\eta\pi^+\pi^-$ ($\pm 10 \text{ MeV}/c^2$ mass window) and $\gamma\pi^+\pi^-$ ($\pm 15 \text{ MeV}/c^2$ mass window) decay modes ($\sim 2.0\sigma$ in each case). A mass- and vertex-constrained fit is applied to η and η' candidates.

D_s^+ candidates are reconstructed using six decay modes: $K_S^0K^+$, $K^-K^+\pi^+$, $K^-K^+\pi^+\pi^0$, $K_S^0K^-\pi^+\pi^+$,

$\eta\pi^+$ and $\eta'\pi^+$. Before calculation of the D_s^+ candidate mass, a vertex fit to a common vertex is performed for tracks that form the D_s^+ candidate. A $\pm 15 \text{ MeV}/c^2$ mass signal window is used for all modes ($\sim 3\sigma$ in each case). To improve the momentum resolution of D_s^+ meson candidates, the tracks from the D_s^+ candidate are fitted to a common vertex with a mass D_s^+ mass constraint. D_s^{*+} candidates are reconstructed using the $D_s^+\gamma$ decay mode. A $\pm 15 \text{ MeV}/c^2$ mass window is used ($\sim 2.5\sigma$). A mass-constrained fit is also applied to D_s^{*+} candidates.

The D_s^+ and D_s^{*+} sidebands used for background studies are four times as large as the signal region and are divided into windows of the same width as that of the signal. To avoid signal over-subtraction, the selected sidebands are shifted by $30 \text{ MeV}/c^2$ from the signal region. The $D_s(D_s^*)$ candidates from these sidebands are refitted to the central mass value of each window.

The $M_{\text{recoil}}^2(D_s^+D_s^-)$ distribution for $M_{D_s^+D_s^-} < 5.0 \text{ GeV}/c^2$ after all the requirements described above is shown in Fig. 1 a). A clear peak corresponding to the $e^+e^- \rightarrow D_s^+D_s^-\gamma_{\text{ISR}}$ process is evident near zero recoil mass. The shoulder at positive values is mainly due to $e^+e^- \rightarrow D_s^+D_s^{*-}\gamma_{\text{ISR}}$ background. We define the signal region with an asymmetric requirement $-0.7(\text{GeV}/c^2)^2 < M_{\text{recoil}}^2(D_s^+D_s^-) < 0.4(\text{GeV}/c^2)^2$ to suppress event this background. The polar angle distribution of the $D_s^+D_s^-$ combinations and the mass spectrum of the $D_s^+D_s^-\gamma_{\text{ISR}}$ combinations (after subtraction of $E_{\text{c.m.}}$) in case (2), after $M_{\text{recoil}}^2(D_s^+D_s^-)$ requirement, are shown in Figs. 1 b,c). These distributions are in agreement with a MC simulation and are typical of ISR production. The $M_{D_s^+D_s^-}$ spectrum with all the requirements applied is shown in Fig. 1 d). A clear peak is seen at threshold near the $\psi(4040)$ mass.

The $M_{\text{recoil}}^2(D_s^+D_s^{*-})$ distribution for $M_{D_s^+D_s^{*-}} < 5.0 \text{ GeV}/c^2$ after all the requirements are applied is shown in Fig. 2 a). A clear peak corresponding to $e^+e^- \rightarrow D_s^+D_s^{*-}\gamma_{\text{ISR}}$ signal process is again evident around zero. We define the signal region for $M_{\text{recoil}}^2(D_s^+D_s^{*-})$ by a requirement $\pm 0.7(\text{GeV}/c^2)^2$ around zero. The polar angle distribution of the $D_s^+D_s^{*-}$ combinations and the mass spectrum of $D_s^+D_s^{*-}\gamma_{\text{ISR}}$ combinations (after subtraction of the $E_{\text{c.m.}}$ energy) in case (2) after the requirement on $M_{\text{recoil}}^2(D_s^+D_s^{*-})$ is applied are shown in Figs. 2 b,c). The $M_{D_s^+D_s^{*-}}$ spectrum after all the requirements are applied is shown in Fig. 2 d). Two clear peaks are seen at the $\psi(4160)$ and the $\psi(4415)$ masses.

The $M_{\text{recoil}}^2(D_s^{*+}D_s^{*-})$ distribution for $M_{D_s^{*+}D_s^{*-}} < 5.0 \text{ GeV}/c^2$ after all the requirements applied is shown in Fig. 3 a). A peak corresponding to $e^+e^- \rightarrow D_s^{*+}D_s^{*-}\gamma_{\text{ISR}}$ is again evident around zero recoil mass. We define the signal region for $M_{\text{recoil}}^2(D_s^{*+}D_s^{*-})$ by a requirement $\pm 0.7(\text{GeV}/c^2)^2$ around zero recoil mass. The polar angle distribution of the $D_s^{*+}D_s^{*-}$ combinations and the mass spectrum of the $D_s^{*+}D_s^{*-}\gamma_{\text{ISR}}$ combinations (after subtraction of $E_{\text{c.m.}}$) that survive the $M_{\text{recoil}}^2(D_s^{*+}D_s^{*-})$ requirement in case (2) are shown in Figs. 3 b,c). The

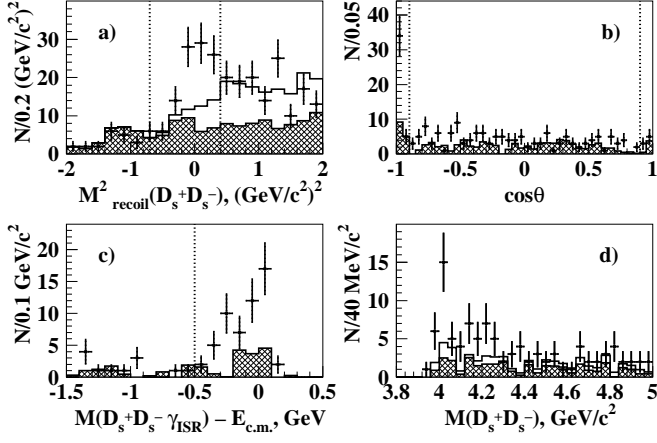


FIG. 1: a) The distribution of $M^2_{\text{recoil}}(D_s^+ D_s^-)$ for $M_{D_s^+ D_s^-} < 5.0 \text{ GeV}/c^2$ after all the requirements are applied. b) The polar angle distribution of the $D_s^+ D_s^-$ combinations. c) The mass spectrum of the $D_s^+ D_s^- \gamma_{\text{ISR}}$ combinations after subtraction of $E_{\text{c.m.}}$ energy in case (2). d) The $M_{D_s^+ D_s^-}$ spectrum after all the requirements applied. Cross-hatched histograms show the normalized $M_{D_s^+}$ and $M_{D_s^-}$ sideband contributions. Feed down from the $D_s^+ D_s^{*-}$ final state is shown by the open histograms. The signal windows are shown by vertical dashed lines.

full $M_{D_s^+ D_s^{*-}}$ spectrum after all the requirements are applied is shown in Fig. 3 d). With such limited statistics no structures are evident.

The contribution of multiple entries after all the requirements is found to be $\sim 6\%$, $\sim 22\%$, $\sim 23\%$, for the $D_s^+ D_s^-$, $D_s^+ D_s^{*-}$ and the $D_s^{*+} D_s^{*-}$ final states, respectively. In such cases, only one $D_s^{(*)+} D_s^{(*)-}$ combination per event, that with the minimum value of $\chi^2_{\text{tot}} = \chi^2_{M(D_s^+)} + \chi^2_{M(D_s^-)} + (\chi^2_{M(D_s^{*+})} + \chi^2_{M(D_s^{*-})})$, is used, where $\chi^2_{M(D_s^+)}$, $\chi^2_{M(D_s^-)}$, $\chi^2_{M(D_s^{*+})}$ and $\chi^2_{M(D_s^{*-})}$ correspond to the mass fits for the D_s^+ , D_s^- , D_s^{*+} and the D_s^{*-} candidates.

The following sources of background are considered: (1) combinatorial background under the $D_s^{(*)+}(D_s^{*-})$ peak combined with a correctly reconstructed $D_s^{(*)-}(D_s^{*+})$ from the signal or other processes; (2) both the $D_s^{(*)+}$ and the $D_s^{(*)-}$ are combinatorial; (3) for the $D_s^+ D_s^-$ final state: reflections from the $e^+ e^- \rightarrow D_s^+ D_s^{*-} \gamma_{\text{ISR}}$ and $e^+ e^- \rightarrow D_s^{*+} D_s^{*-} \gamma_{\text{ISR}}$ processes followed by $D_s^* \rightarrow D_s \gamma$, where the low momentum γ is not reconstructed; for the $D_s^+ D_s^{*-}$ final state: reflection from the $e^+ e^- \rightarrow D_s^{*+} D_s^{*-} \gamma_{\text{ISR}}$ process followed by $D_s^* \rightarrow D_s \gamma$, where the low momentum γ is not reconstructed; (4) reflection from the $e^+ e^- \rightarrow D_s^{(*)+} D_s^{(*)-} \pi^0_{\text{miss}} \gamma_{\text{ISR}}$ processes, where the π^0_{miss} is not reconstructed. (5) the contribution of $e^+ e^- \rightarrow D_s^{(*)+} D_s^{(*)-} \pi^0$, when an energetic π^0 is misidentified as a single γ_{ISR} .

The contribution from background (1) is extracted using the $D_s^{(*)-}$ and $D_s^{(*)+}$ sidebands. Background (2) is

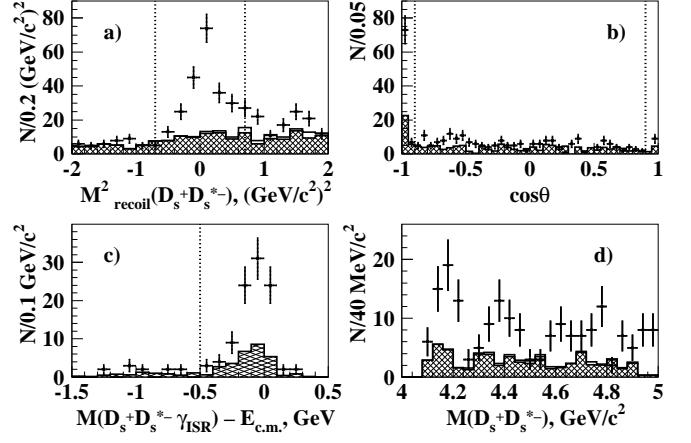


FIG. 2: a) The distribution of the $M^2_{\text{recoil}}(D_s^+ D_s^{*-})$ for $M_{D_s^+ D_s^{*-}} < 5.0 \text{ GeV}/c^2$ after all the requirements applied. b) The polar angle distribution of the $D_s^+ D_s^{*-}$ combinations. c) The mass spectrum of the $D_s^+ D_s^{*-} \gamma_{\text{ISR}}$ combinations after subtraction of $E_{\text{c.m.}}$ in case (2). d) The obtained $M_{D_s^+ D_s^{*-}}$ spectrum. Cross-hatched histograms show the normalized $M_{D_s^+}$ and $M_{D_s^{*-}}$ sidebands contributions. The small contamination from the $D_s^{*+} D_s^{*-}$ final state is shown by the open histograms. The signal windows are shown by vertical dashed lines.

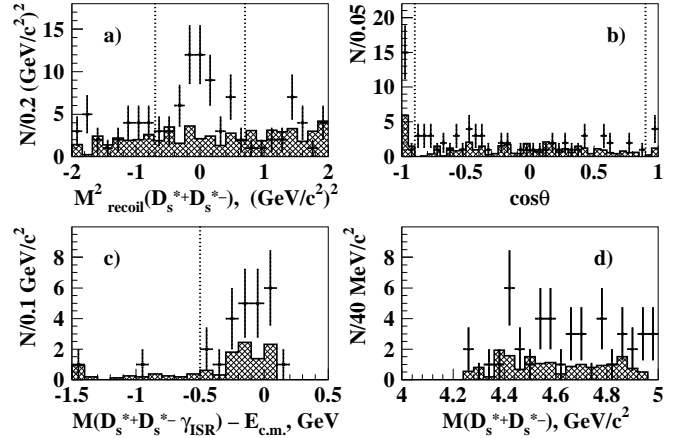


FIG. 3: a) The distributions of the $M^2_{\text{recoil}}(D_s^{*+} D_s^{*-})$ for $M_{D_s^{*+} D_s^{*-}} < 5.0 \text{ GeV}/c^2$ after all the requirements applied. b) The polar angle distribution of the $D_s^{*+} D_s^{*-}$ combinations. c) The mass spectrum of the $D_s^{*+} D_s^{*-} \gamma_{\text{ISR}}$ combinations after subtraction of $E_{\text{c.m.}}$ in case (2). d) The $M_{D_s^{*+} D_s^{*-}}$ spectrum after all the requirements applied. Cross-hatched histograms show the normalized $M_{D_s^{*+}}$ and $M_{D_s^{*-}}$ sidebands contributions. The signal windows are shown by vertical dashed lines.

present in both the $M_{D_s^{(*)+}}$ and $M_{D_s^{(*)-}}$ sidebands and is, thus, subtracted twice. To account for this over-subtraction we use a double sideband region, when events are selected from both the $M_{D_s^{(*)+}}$ and the $M_{D_s^{(*)-}}$ sidebands. The contributions from the combinatorial backgrounds (1-2) are shown in Figs. 1 d) and 2 d) as cross-

hatched histograms.

Backgrounds (3–4) are suppressed by the tight requirement on $M_{\text{recoil}}^2(D_s^{(*)+}D_s^{(*)-})$. The remaining background (3) for the $D_s^+D_s^{*-}$ final state is estimated using a MC simulation of the $e^+e^- \rightarrow D_s^{*+}D_s^{*-}\gamma_{\text{ISR}}$ process. To reproduce the shape of the $D_s^+D_s^{*-}$ mass spectrum we use the initial measurement of the $D_s^{*+}D_s^{*-}$ mass spectrum. The remainder of background (3) for the $D_s^+D_s^-$ final state is estimated using a MC simulation of the $e^+e^- \rightarrow D_s^+D_s^{*-}\gamma_{\text{ISR}}$ and $e^+e^- \rightarrow D_s^{*+}D_s^{*-}\gamma_{\text{ISR}}$ processes. To reproduce the shape of the $D_s^+D_s^-$ mass spectrum we use the initial measurement of the $D_s^{*+}D_s^{*-}$ mass spectrum and the first iteration of the $D_s^+D_s^{*-}$ mass spectrum. The contributions from background (3) for the $D_s^+D_s^-$ and the $D_s^+D_s^{*-}$ final states are shown in Figs. 1 a), 1 d) and Figs. 2 a), 2 d) as open histograms. Uncertainties in these estimates are included in the systematic errors.

To estimate the contribution from background (4), we study the $e^+e^- \rightarrow D_s^{(*)+}D_s^{(*)-}\pi^0\gamma_{\text{ISR}}$ processes using fully reconstructed final states. From a MC study we estimate the fraction of reconstructed events for the cases where the π^0 is not detected. After the application of the requirement on $M_{\text{recoil}}^2(D_s^{(*)+}D_s^{(*)-})$ this contribution is found to be less than 0.5% and negligibly small; uncertainties in this estimate are included in the systematic errors.

The contribution from background (5), in which an energetic π^0 is misidentified as the γ_{ISR} candidate, is determined from the data using fully reconstructed $e^+e^- \rightarrow D_s^{(*)+}D_s^{(*)-}\pi^0$ events. Only three events with $M_{D_s^+D_s^-} < 5.0 \text{ GeV}/c^2$ and $M_{D_s^+D_s^-}\pi^0 - E_{\text{c.m.}} > 0.5 \text{ GeV}$ are found in the data. Assuming a uniform π^0 polar angle distribution, this background contribution in the $|\cos(\theta_{D_s^+D_s^-})| > 0.9$ signal sub-sample (case 1) is 3 events/ $9\epsilon_{\pi^0} \sim 0.6$ events in the whole $M_{D_s^+D_s^-}$ mass range, where ϵ_{π^0} is the π^0 reconstruction efficiency. For the $D_s^+D_s^{*-}$ and the $D_s^{*+}D_s^{*-}$ final states the expected backgrounds are ~ 0.6

events and 0 events in the whole $M_{D_s^+D_s^{*-}}$ and $M_{D_s^{*+}D_s^{*-}}$ mass ranges. The probability of $\pi^0 \rightarrow \gamma\gamma$ misidentification due to asymmetric $\pi^0 \rightarrow \gamma\gamma$ decays is also estimated to be small. Thus the contribution from background (5) is found to be negligibly small; uncertainties in these estimates are included in the systematic error.

The $e^+e^- \rightarrow D_s^{(*)+}D_s^{(*)-}$ cross sections are extracted from the background subtracted $D_s^{(*)+}D_s^{(*)-}$ mass distributions

$$\sigma(e^+e^- \rightarrow D_s^{(*)+}D_s^{(*)-}) = \frac{dN/dm}{\eta_{\text{tot}}dL/dm}, \quad (2)$$

where $m \equiv M_{D_s^{(*)+}D_s^{(*)-}}$, dN/dm is the obtained mass spectrum, η_{tot} is the total efficiency [17]. The factor dL/dm is the differential ISR luminosity:

$$dL/dm = \frac{\alpha}{\pi x} \left((2 - 2x + x^2) \ln \frac{1+C}{1-C} - x^2 C \right) \frac{2m\mathcal{L}}{E_{\text{c.m.}}^2}, \quad (3)$$

where $x = 1 - m^2/E_{\text{c.m.}}^2$, \mathcal{L} is the total integrated luminosity and $C = \cos\theta_0$, where θ_0 denotes the polar angle range for γ_{ISR} in the e^+e^- c.m. frame: $\theta_0 < \theta_{\gamma_{\text{ISR}}} < 180 - \theta_0$. The total efficiencies determined by the MC simulation grow quadratically with energy from 0.015%, 0.010%, 0.005% near threshold to 0.045%, 0.025%, 0.011% at $5.0 \text{ GeV}/c^2$ for the $D_s^+D_s^-$, $D_s^+D_s^{*-}$ and the $D_s^{*+}D_s^{*-}$ final states, respectively. The resulting $e^+e^- \rightarrow D_s^{(*)+}D_s^{(*)-}$ exclusive cross sections averaged over the bin width are shown in Fig. 4. Since the bin width is much larger than the $M_{D_s^{(*)+}D_s^{(*)-}}$ resolution, which varies from $\sim 2 \text{ MeV}/c^2$ around threshold to $\sim 6 \text{ MeV}/c^2$ at $M_{D_s^{(*)+}D_s^{(*)-}} = 5.0 \text{ GeV}/c^2$, no correction for resolution is applied. The next-to-leading order radiative corrections are taken into account by the dL/dm formula. The next-to-next-to-leading order corrections are included in the systematics. The contribution of final state radiation (FSR) is strongly suppressed [18] and is neglected in this study.

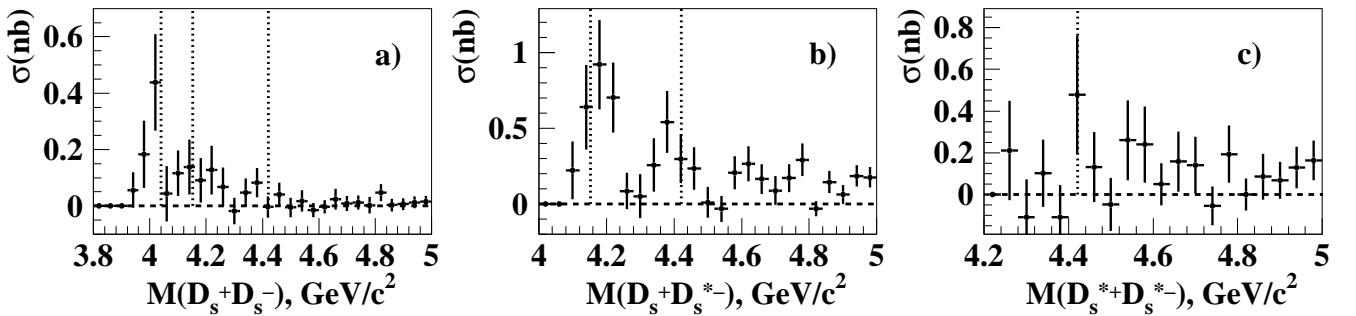


FIG. 4: The cross section averaged over the bin width for a) the $e^+e^- \rightarrow D_s^+D_s^-$ process; b) the $e^+e^- \rightarrow D_s^+D_s^{*-} + \text{c.c.}$ process; c) the $e^+e^- \rightarrow D_s^{*+}D_s^{*-}$ process. Error bars show statistical uncertainties only. There is a common systematic uncertainty for all measurements, 11% for $D_s^+D_s^-$, 17% for $D_s^+D_s^{*-}$ and 31% for $D_s^{*+}D_s^{*-}$. This uncertainty is described in the text. The dotted lines show masses of the $\psi(4040)$, $\psi(4160)$ and $\psi(4415)$ states [16].

The R ratio, defined as $R = \sigma(e^+e^- \rightarrow \text{hadrons})/\sigma(e^+e^- \rightarrow \mu^+\mu^-)$, where $\sigma(e^+e^- \rightarrow \mu^+\mu^-) =$

$4\pi\alpha^2/3s$, for the sum of the exclusive $e^+e^- \rightarrow D_s^{(*)+}D_s^{(*)-}$ cross sections is shown in Fig. 5.

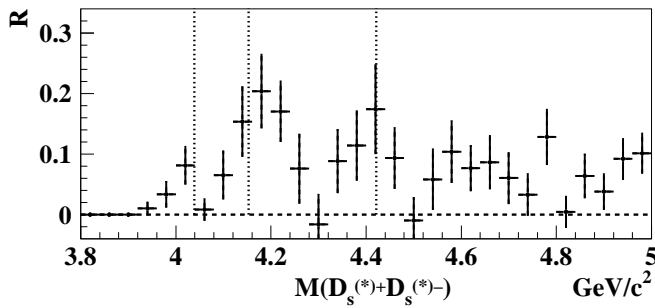


FIG. 5: The R ratio for the sum of the $D_s^+D_s^-$, $D_s^+D_s^{*-}$ and the $D_s^{*+}D_s^{*-}$ final states. The vertical dotted lines show the masses of the $\psi(4040)$, $\psi(4160)$ and $\psi(4415)$ states [16]. Error bars show statistical uncertainties only.

The systematic errors for the $\sigma(e^+e^- \rightarrow D_s^{(*)+}D_s^{(*)-})$ measurements are summarized in Table I. The system-

TABLE I: Contributions to the systematic error on the cross sections.

Source	$D_s^+D_s^-$	$D_s^+D_s^{*-}$	$D_s^{*+}D_s^{*-}$
Background subtraction	$\pm 4\%$	$\pm 7\%$	$\pm 24\%$
Cross section calculation	$\pm 7\%$	$\pm 11\%$	$\pm 12\%$
$\mathcal{B}(D_s^{(*)})$	$\pm 5\%$	$\pm 5\%$	$\pm 5\%$
Reconstruction	$\pm 6\%$	$\pm 10\%$	$\pm 16\%$
Kaon identification	$\pm 2\%$	$\pm 2\%$	$\pm 2\%$
Total	$\pm 11\%$	$\pm 17\%$	$\pm 31\%$

atic errors associated with the background (1–2) subtraction are estimated from the uncertainty in the scaling factors for the sideband subtractions. This is done using fits to the $M_{D_s^{(*)+}}$ and $M_{D_s^{(*)-}}$ distributions in the data with different signal and background parameterizations and are found to be 3%, 7% and 24% for the $D_s^+D_s^-$, $D_s^+D_s^{*-}$ and the $D_s^{*+}D_s^{*-}$ final states, respectively. Uncertainties in the contribution from background (3) are estimated to be 2% for the $D_s^+D_s^-$ final state and smaller than 1% for the $D_s^+D_s^{*-}$ final state. Uncertainties in the backgrounds (4–5) are estimated conservatively to be smaller than 1% of the signal for all final states. The systematic errors ascribed to the cross section calculation include an error on the differential ISR luminosity (2%) and statistical errors of the MC simulation for the total efficiency calculations. In the case of the $D_s^+D_s^{*-}$ state there is an additional uncertainty due to the unknown helicity distribution, estimated following a procedure similar to that used in Ref [3]. Another source of systematic error comes from the uncertainties in track and photon reconstruction efficiencies (1% per track, 1.5% per photon and 7% per soft photon). Other contributions include the uncertainty in the identification efficiency and the absolute

D_s^+ and D_s^{*+} branching fractions [16]. The total systematic uncertainties are 11%, 17% and 31% for the $D_s^+D_s^-$, $D_s^+D_s^{*-}$ and the $D_s^{*+}D_s^{*-}$ final states, respectively.

In summary, we report the measurement of the $e^+e^- \rightarrow D_s^{(*)+}D_s^{(*)-}$ exclusive cross sections over the center-of-mass energy range from the $D_s^{(*)+}D_s^{(*)-}$ thresholds to 5.0 GeV. A clear peak at threshold around the $\psi(4040)$ mass is seen in the $e^+e^- \rightarrow D_s^+D_s^-$ cross section. In the $e^+e^- \rightarrow D_s^+D_s^{*-}$ cross section two peaks are evident around the $\psi(4160)$ and the $\psi(4415)$ masses. The limited statistics do not reveal any structures in the $e^+e^- \rightarrow D_s^{*+}D_s^{*-}$ cross section. The obtained R ratio for the sum of $e^+e^- \rightarrow D_s^{(*)+}D_s^{(*)-}$ cross sections has a rich structure including peaks around the $\psi(4040)$, $\psi(4160)$ and the $\psi(4415)$ masses. Both the $e^+e^- \rightarrow D_s^+D_s^{*-}$ cross section and the R ratio exhibit an obvious dip near the $Y(4260)$ mass, similar to what is seen in $e^+e^- \rightarrow D^*\bar{D}^*$ and in the total cross section for charm production. The obtained cross sections are consistent within errors with those from BaBar [10]. The CLEO exclusive cross sections [9] are not radiatively corrected and, therefore, cannot be directly compared to the results reported here.

In this study we do not perform a fit to the obtained $e^+e^- \rightarrow D_s^{(*)+}D_s^{(*)-}$ cross sections. The numerous open charm thresholds in this region complicate the cross sections behavior and coupled-channel modifications to the description of any particular final state require one to take into account all other final states contributing to the total cross section for charm production.

We thank the KEKB group for the excellent operation of the accelerator, the KEK cryogenics group for the efficient operation of the solenoid, and the KEK computer group and the National Institute of Informatics for valuable computing and SINET3 network support. We acknowledge support from the Ministry of Education, Culture, Sports, Science, and Technology (MEXT) of Japan, the Japan Society for the Promotion of Science (JSPS), and the Tau-Lepton Physics Research Center of Nagoya University; the Australian Research Council and the Australian Department of Industry, Innovation, Science and Research; the National Natural Science Foundation of China under contract No. 10575109, 10775142, 10875115 and 10825524; the Ministry of Education, Youth and Sports of the Czech Republic under contract No. LA10033 and MSM0021620859; the Department of Science and Technology of India; the BK21 and WCU program of the Ministry Education Science and Technology, National Research Foundation of Korea, and NSDC of the Korea Institute of Science and Technology Information; the Polish Ministry of Science and Higher Education; the Ministry of Education and Science of the Russian Federation and the Russian Federal Agency for Atomic Energy; the Slovenian Research Agency; the Swiss National Science Foundation; the National Science Council and the Ministry of Education of Taiwan; and the U.S. Department of Energy. This work is supported by a Grant-in-Aid from MEXT for Science

Research in a Priority Area (“New Development of Flavor Physics”), and from JSPS for Creative Scientific Re-

search (“Evolution of Tau-lepton Physics”).

-
- [1] Charge-conjugate modes are included throughout this paper.
 - [2] G. Pakhlova *et al.* (Belle Collab.), Phys. Rev. D **77**, 011103 (2008).
 - [3] G. Pakhlova *et al.* (Belle Collab.), Phys. Rev. Lett. **98**, 092001 (2007).
 - [4] G. Pakhlova *et al.* (Belle Collab.), Phys. Rev. Lett. **100**, 062001 (2008).
 - [5] G. Pakhlova *et al.* (Belle Collab.), Phys. Rev. D **80**, 091101 (2009).
 - [6] G. Pakhlova *et al.* (Belle Collab.), Phys. Rev. Lett. **101**, 172001 (2008).
 - [7] B. Aubert *et al.* (BaBar Collab.), Phys. Rev. D **76**, 111105 (2007).
 - [8] B. Aubert *et al.* (BaBar Collab.), Phys. Rev. D **79**, 092001 (2009).
 - [9] D. Cronin-Hennessy *et al.* (CLEO Collab.), Phys. Rev. D **80**, 072001 (2009).
 - [10] P. del Amo Sanchez *et al.* (BaBar Collab.), Phys. Rev. D **82**, 052004 (2010).
 - [11] M. Ablikim *et al.* (BES Collab.), Phys. Lett. B **660**, 315 (2008).
 - [12] B. Aubert *et al.* (BaBar Collab.), Phys. Rev. Lett. **95**, 142001 (2005); T. E. Coan *et al.* (CLEO Collab.), Phys. Rev. Lett. **96**, 162003 (2006); Q. He *et al.* (CLEO Collab.), Phys. Rev. D **74**, 091104 (2006); C. Z. Yuan *et al.* (Belle Collab.), Phys. Rev. Lett. **99**, 182004 (2007); B. Aubert *et al.* (BaBar Collab.), arXiv:0808.1543 [hep-ex], (2008); B. Aubert *et al.* (BaBar Collab.), Phys. Rev. Lett. **98**, 212001 (2007); X. L. Wang *et al.* (Belle Collab.), Phys. Rev. Lett. **99**, 142002 (2007); Z. Q. Liu, X. S. Qin and C. Z. Yuan, Phys. Rev. D **78**, 014032 (2008).
 - [13] A. Abashian *et al.* (Belle Collaboration), Nucl. Instr. and Meth. A **479**, 117 (2002).
 - [14] S. Kurokawa and E. Kikutani, Nucl. Instr. and Meth. A **499**, 1 (2003); and other papers included in this volume.
 - [15] E. Nakano, Nucl. Instrum. Meth., A **494**, 402 (2002).
 - [16] K. Nakamura *et al.* (Particle Data Group), J. Phys. G **37**, 075021 (2010).
 - [17] E. A. Kuraev and V. S. Fadin, Sov. J. Nucl. Phys. **41**, 466 (1985) [Yad. Fiz **41**, 733 (1985)].
 - [18] S. Actis *et al.*, Eur. Phys. J. C **66**, 585 (2010).